Research Article | Vol. 26, No. 12 | 11 Jun 2018 | OPTICS EXPRESS 15759
Optics EXPRESS

Three-dimensional super-resolution correlation-differential confocal microscopy with nanometer axial focusing accuracy

WEIQIAN ZHAO,[1] YINGBIN SUN,[1] YUN WANG,[1,*] LIRONG QIU,[1] RONGJUN SHAO,[1] AND HAN CUI[1,2]

[1]*Beijing Key Laboratory for Precision Optoelectronic Measurement Instrument and Technology, School of Optics and Photonics, Beijing Institute of Technology, Beijing 100081, China*
[2]*Division of Biomedical Engineering, School of Engineering, University of Glasgow, Glasgow G12 8LT, UK*
[*]*wangyun_19840703@163.com*

Abstract: We present a correlation-differential confocal microscopy (CDCM), a novel method that can simultaneously improve the three-dimensional spatial resolution and axial focusing accuracy of confocal microscopy (CM). CDCM divides the CM imaging light path into two paths, where the detectors are before and after the focus with an equal axial offset in opposite directions. Then, the light intensity signals received from the two paths are processed by the correlation product and differential subtraction to improve the CM spatial resolution and axial focusing accuracy, respectively. Theoretical analyses and preliminary experiments indicate that, for the excitation wavelength of λ = 405 nm, numerical aperture of NA = 0.95, and the normalized axial offset of u_M = 5.21, the CDCM resolution is improved by more than 20% and more than 30% in the lateral and axial directions, respectively, compared with that of the CM. Also, the axial focusing resolution important for the imaging of sample surface profiles is improved to 1 nm.

OCIS codes: (120.6650) Surface measurements, figure; (120.4800) Optical standards and testing; (180.1790) Confocal microscopy; (180.6900) Three-dimensional microscopy.

References and links

1. J. G. White and W. B. Amos, "Confocal microscopy comes of age," Nature **328**(6126), 183–184 (1987).
2. A. E. Dixon, S. Damaskinos, and M. R. Atkinson, "A scanning confocal microscope for transmission and reflecting imaging," Nature **351**(6327), 551–553 (1991).
3. G. J. Puppels, F. F. M. de Mul, C. Otto, J. Greve, M. Robert-Nicoud, D. J. Arndt-Jovin, and T. M. Jovin, "Studying single living cells and chromosomes by confocal Raman microspectroscopy," Nature **347**(6290), 301–303 (1990).
4. G. Scarcelli and S. H. Yun, "Confocal Brillouin microscopy for three-dimensional mechanical imaging," Nat. Photonics **2**(1), 39–43 (2007).
5. S. W. Hell, S. J. Sahl, M. Bates, X. Zhuang, R. Heintzmann, M. J. Booth, J. Bewersdorf, G. Shtengel, H. Hess, P. Tinnefeld, A. Honigmann, S. Jakobs, I. Testa, L. Cognet, B. Lounis, H. Ewers, S. J. Davis, C. Eggeling, D. Klenerman, K. I. Willig, G. Vicidomini, M. Castello, A. Diaspro, and T. Cordes, "The 2015 super-resolution microscopy roadmap," J. Phys. D Appl. Phys. **48**(44), 443001 (2015).
6. B. Huang, H. Babcock, and X. Zhuang, "Breaking the Diffraction Barrier: Super-Resolution Imaging of Cells," Cell **143**(7), 1047–1058 (2010).
7. S. W. Hell and J. Wichmann, "Breaking the diffraction resolution limit by stimulated emission: stimulated-emission-depletion fluorescence microscopy," Opt. Lett. **19**(11), 780–782 (1994).
8. S. W. Hell, "Far-Field Optical Nanoscopy," Science **316**(5828), 1153–1158 (2007).
9. M. G. L. Gustafsson, "Nonlinear structured-illumination microscopy: wide-field fluorescence imaging with theoretically unlimited resolution," Proc. Natl. Acad. Sci. U.S.A. **102**(37), 13081–13086 (2005).
10. E. Betzig, G. H. Patterson, R. Sougrat, O. W. Lindwasser, S. Olenych, J. S. Bonifacino, M. W. Davidson, J. Lippincott-Schwartz, and H. F. Hess, "Imaging Intracellular Fluorescent Proteins at Nanometer Resolution," Science **313**(5793), 1642–1645 (2006).
11. M. J. Rust, M. Bates, and X. Zhuang, "Sub-diffraction-limit imaging by stochastic optical reconstruction microscopy (STORM)," Nat. Methods **3**(10), 793–795 (2006).
12. M. Bates, B. Huang, G. T. Dempsey, and X. Zhuang, "Multicolor Super-Resolution Imaging with Photo-Switchable Fluorescent Probes," Science **317**(5845), 1749–1753 (2007).
13. S. Hell and E. H. K. Stelzer, "Properties of a 4Pi confocal fluorescence microscope," J. Opt. Soc. Am. A **9**(12), 2159–2166 (1992).

#327390 https://doi.org/10.1364/OE.26.015759
Journal © 2018 Received 2 Apr 2018; revised 25 May 2018; accepted 27 May 2018; published 7 Jun 2018

Optics EXPRESS

14. S. Hell, S. Lindek, C. Cremer, and E. H. K. Stelzer, "Measurement of the 4Pi-confocal point spread function proves 75 nm axial resolution," Appl. Phys. Lett. **64**(11), 1335–1337 (1994).
15. P. E. Hänninen, S. W. Hell, J. Salo, E. Soini, and C. Cremer, "Two-photon excitation 4Pi confocal microscope: Enhanced axial resolution microscope for biological research," Appl. Phys. Lett. **66**(13), 1698–1700 (1995).
16. C. J. Sheppard and D. K. Hamilton, "High resolution stereoscopic imaging," Appl. Opt. **22**(6), 886–887 (1983).
17. C. J. Sheppard, W. Gong, and K. Si, "The divided aperture technique for microscopy through scattering media," Opt. Express **16**(21), 17031–17038 (2008).
18. Y. Ma, C. Kuang, W. Gong, L. Xue, Y. Zheng, Y. Wang, K. Si, and X. Liu, "Improvements of axial resolution in confocal microscopy with fan-shaped apertures," Appl. Opt. **54**(6), 1354–1362 (2015).
19. E. H. K. Stelzer and S. Lindek, "Fundamental reduction of the observation volume in far-field light microscopy by detection orthogonal to the illumination axis: confocal theta microscopy," Opt. Commun. **111**(5–6), 536–547 (1994).
20. S. Lindek, C. Cremer, and E. H. K. Stelzer, "Confocal theta fluorescence microscopy with annular apertures," Appl. Opt. **35**(1), 126–130 (1996).
21. P. J. Dwyer, C. A. DiMarzio, J. M. Zavislan, W. J. Fox, and M. Rajadhyaksha, "Confocal reflectance theta line scanning microscope for imaging human skin in vivo," Opt. Lett. **31**(7), 942–944 (2006).
22. T. D. Wang, M. J. Mandella, C. H. Contag, and G. S. Kino, "Dual-axis confocal microscope for high-resolution in vivo imaging," Opt. Lett. **28**(6), 414–416 (2003).
23. H. Ra, W. Piyawattanametha, M. J. Mandella, P.-L. Hsiung, J. Hardy, T. D. Wang, C. H. Contag, G. S. Kino, and O. Solgaard, "Three-dimensional in vivo imaging by a handheld dual-axes confocal microscope," Opt. Express **16**(10), 7224–7232 (2008).
24. D. Wang, D. Meza, Y. Wang, L. Gao, and J. T. C. Liu, "Sheet-scanned dual-axis confocal microscopy using Richardson-Lucy deconvolution," Opt. Lett. **39**(18), 5431–5434 (2014).
25. D. Kang and D. Gweon, "Enhancement of lateral resolution in confocal self-interference microscopy," Opt. Lett. **28**(24), 2470–2472 (2003).
26. S. Pechprasarn, B. Zhang, D. Albutt, J. Zhang, and M. Somekh, "Ultrastable embedded surface plasmon confocal interferometry," Light Sci. Appl. **3**(7), e187 (2014).
27. M. Gu, T. Tannous, and C. J. R. Sheppard, "Improved axial resolution in confocal fluorescence microscopy using annular pupils," Opt. Commun. **110**(5–6), 533–539 (1994).
28. W. Zhao, L. Qiu, and Z. Feng, "Effect of fabrication errors on superresolution property of a pupil filter," Opt. Express **14**(16), 7024–7036 (2006).
29. R. Dorn, S. Quabis, and G. Leuchs, "Sharper focus for a radially polarized light beam," Phys. Rev. Lett. **91**(23), 233901 (2003).
30. W. T. Tang, E. Y. Yew, and C. J. R. Sheppard, "Polarization conversion in confocal microscopy with radially polarized illumination," Opt. Lett. **34**(14), 2147–2149 (2009).
31. Q. Zhan, "Cylindrical vector beams: from mathematical concepts to applications," Adv. Opt. Photonics **1**(1), 1–57 (2009).
32. C. H. Lee, H. Y. Chiang, and H. Y. Mong, "Sub-diffraction-limit imaging based on the topographic contrast of differential confocal microscopy," Opt. Lett. **28**(19), 1772–1774 (2003).
33. W. Lu, M. Chang, P. C. Chen, and W. M. Luo, "Iterative deconvolution technique for measurements of diffraction-limited images on optical microscopes," J. Mod. Opt. **61**(sup1), S2–S9 (2014).
34. M. G. Gustafsson, "Surpassing the lateral resolution limit by a factor of two using structured illumination microscopy," J. Microsc. **198**(Pt 2), 82–87 (2000).
35. C. Zhang, C. Min, L. Du, and X.-C. Yuan, "Perfect optical vortex enhanced surface plasmon excitation for plasmonic structured illumination microscopy imaging," Appl. Phys. Lett. **108**(20), 201601 (2016).
36. M. Saxena, G. Eluru, and S. S. Gorthi, "Structured illumination microscopy," Adv. Opt. Photonics **7**(2), 241–275 (2015).
37. C. J. R. Sheppard, "Super-resolution in confocal imaging," Optik (Stuttg.) **80**(2), 53–54 (1988).
38. C. B. Müller and J. Enderlein, "Image scanning microscopy," Phys. Rev. Lett. **104**(19), 198101 (2010).
39. W. Zhao, Q. Jiang, L. Qiu, and D. Liu, "Dual-axes differential confocal microscopy with high axial resolution and long working distance," Opt. Commun. **284**(1), 15–19 (2011).
40. W. Zhao, C. Liu, and L. Qiu, "Laser divided-aperture differential confocal sensing technology with improved axial resolution," Opt. Express **20**(23), 25979–25989 (2012).
41. Y. Tan, W. Wang, C. Xu, and S. Zhang, "Laser confocal feedback tomography and nano-step height measurement," Sci. Rep. **3**(43), 2971 (2013).
42. O. Schwartz and D. Oron, "Improved resolution in fluorescence microscopy using quantum correlations," Phys. Rev. A **85**(3), 145–150 (2012).
43. J. M. Cui, F. W. Sun, X. D. Chen, Z. J. Gong, and G. C. Guo, "Quantum statistical imaging of particles without restriction of the diffraction limit," Phys. Rev. Lett. **110**(15), 153901 (2013).
44. Y. Israel, R. Tenne, D. Oron, and Y. Silberberg, "Quantum correlation enhanced super-resolution localization microscopy enabled by a fibre bundle camera," Nat. Commun. **8**, 14786 (2017).
45. H. Shen, L. J. Tauzin, R. Baiyasi, W. Wang, N. Moringo, B. Shuang, and C. F. Landes, "Single Particle Tracking: From Theory to Biophysical Applications," Chem. Rev. **117**(11), 7331–7376 (2017).

Optics EXPRESS

1. Introduction

Confocal microscope (CM) is widely used in various scientific disciplines including physics, chemistry, biomedicine, and materials science, owing to its unique capabilities of optical sectioning and high spatial resolution imaging [1–5]. However, the CM resolution is limited by the diffraction effect to ~200 nm in the lateral direction and 500 nm in the axial direction, which is insufficient for a high spatial resolution imaging. Furthermore, the sample drift has a prominent effect on the CM imaging quality owing to the time-consuming scan method of the point-by-point and layer-by-layer modes.

In recent years, the super-resolution fluorescence imaging technology has been rapidly developed [5–12], and the spatial resolution of far-field optical microscopy have been improved to 50 nm, which is significant for chemical, biophysical, and biomedical applications. However, these super-resolution microscopy techniques can't image non-fluorescently labeled samples, such as MEMS devices, lithography masks, and integrated circuit.

The research on non-fluorescent labeled high-resolution technology is in its initial stage and mainly includes two types. One is changing the optical structures, such as the 4Pi confocal microscopy [13–15], divided-aperture confocal microscopy (DACM) [16–18], confocal theta microscopy (CTM) [19–21], dual-axis confocal microscopy (DCM) [22–24], and confocal self-interference microscopy (CSIM) [25,26], these methods achieve high resolution, such as lateral 120 nm and axial 70 nm of 4 Pi confocal microscopy, 1.3μm and 2.1μm of DCM, but they use complicated structures and are not easy to operate. The other is a combination of CM and the existing super-resolution technology including the pupil filtering technique [27,28], tight focusing technique of a radially polarized light [29–31], super-resolution image restoration algorithm [32,33], structured illumination microscopy (SIM) [34–36], and imaging scanning microscopy (ISM) [37–41], these methods improve lateral resolution significantly but they cannot improve axial resolution simultaneously and cause a serious loss of light intensity. Therefore, the current methods is difficult to simultaneously improve the lateral and axial resolutions of the CM system by simple structural changes, which restrict their engineering applications in the field of practical research and production.

In the past few years, a method that employs non-classical statistics photon correlation to achieve a sub-diffraction-limited imaging has been proposed and verified in fluorescence microscope, CM, localization microscope, and SIM [42–44]. Nevertheless, the degrees of improvement of both lateral and axial resolutions have not been reported.

To improve CM's spatial resolution and sample axial focusing accuracy [45], a novel method called correlation-differential confocal microscopy (CDCM) has been proposed based on the classical photon correlation measurement technique, which provides a nano-precision sample tracking capability and high spatial resolution. CDCM divides the CM imaging light path into two paths, where the detectors are before and after the focus with an equal axial offset in opposite directions. Then, the light intensity signals simultaneously received from these two paths are processed by correlation product and differential subtraction to improve the CM's spatial resolution and axial focusing accuracy respectively, thereby achieving the axial tracking and focusing on the sample at nanometer level. Compared with other non-fluorescent labeled high-resolution technology, such as 4Pi confocal microscopy, DACM, CTM, DCM, and CSIM, CDCM has a simple structure. Therefore, CDCM is a potential method to be used in many fields, such as chemistry, microelectronics, and material science physics

2. Principles

As illustrated in Fig. 1, the measurement principle of CDCM is described as follows. CDCM divides the confocal microscopy light into imaging path before the focus in Fig. 1(a) (dash-dotted area) and imaging path after the focus in Fig. 1(b) (the dashed area). The beam emitted from the laser passes through a beam expander (BE) and polarization beam splitter

Optics EXPRESS

(PBS). The p-polarized light transmits PBS, passes through a quarter-wave plate (QWP) and then is focused onto the sample (S) by the objective L_o. The reflected light transmits along the original light path and passes through the BS_1 after being reflected by the PBS, and then, is divided into two components by a 5:5 beam splitter (BS_2). These two components are focused by the converging lenses L_1 and L_2 with the same parameters and detected by the detectors D_1 and D_2 close to the pinholes P_1 and P_2, respectively. P_1 is before the focal plane of L_1 with a distance of $-u_M$. P_2 is after the focal plane of L_2 with a distance of $+u_M$. The gray background area in Fig. 1(c) illustrates the light path diagram in CM to compare with CDCM.

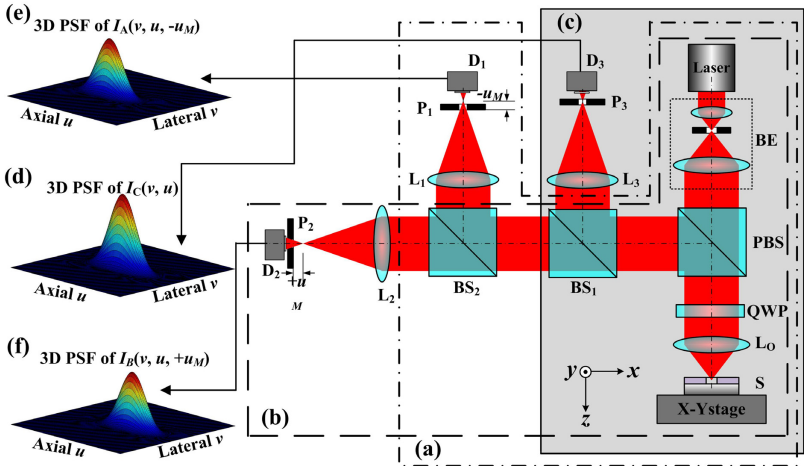

Fig. 1. Schematic of a CDCM measurement. (a) CDCM's imaging path before the focus, (b) CDCM's imaging path after the focus, (c) CM's light path diagram, (d) 3D intensity response I_C (v, u) of CM, (e) 3D intensity response I_A (v, u, $-u_M$) of CDCM's imaging path before the focus, (f) 3D intensity response I_B(v, u, $+u_M$) of CDCM's imaging path after the focus. Here, v is the normalized lateral coordinate, u is the normalized axial coordinate, u_M is the normalized detector axial off-focus offset.

When the sample S is scanned, the intensity response signals received by detectors D_1, D_2, and D_3 are $I_A(v, u, -u_M)$, $I_B(v, u, +u_M)$, and $I_C(v, u)$, respectively. They can be expressed as Eqs. (1)-(3):

$$I_A(v,u,-u_M)=\left|h_i(v,u)\right|^2\cdot\left[\left|h_c(v,u,-u_M)\right|^2\otimes D(v)\right] \tag{1}$$

$$I_B(v,u,+u_M)=\left|h_i(v,u)\right|^2\cdot\left[\left|h_c(v,u,+u_M)\right|^2\otimes D(v)\right] \tag{2}$$

$$I_C(v,u,u_M=0)=\left|h_i(v,u)\right|^2\cdot\left[\left|h_c(v,u,u_M=0)\right|^2\otimes D(v)\right] \tag{3}$$

Where h_i is the illumination point spread function, h_c is the collection point spread function, and $D(v)$ is the normalized intensity response function of detector, h_i, h_c, and $D(v)$ can be expressed as Eqs. (4)-(6):

$$h_i(v,u)=\int_0^{a_0}J_0\left(\frac{v\sin\theta}{\sin a_0}\right)e^{iu\sin^2(\theta/2)/2\sin^2(a_0/2)}\sin\theta\sqrt{\cos\theta}\,d\theta \tag{4}$$

$$h_c(v,u,\mp u_M)=\int_0^{a_0}J_0\left(\frac{v\sin\theta}{\sin a_0}\right)e^{i(u\pm u_M)\sin^2(\theta/2)/2\sin^2(a_0/2)}\sin\theta\sqrt{\cos\theta}\,d\theta \tag{5}$$

Optics EXPRESS

$$D(v)=\delta(u_M)\begin{cases}1, & v\le v_D\\ 0, & \text{else}\end{cases} \tag{6}$$

where J_0 is the zero-order Bessel function, v is the optical normalized coordinate of the lateral coordinate r ($r^2 = x^2 + y^2$) in the object space ($v = 2\pi r\sin(a_0)/\lambda$), u is the optical normalized coordinate of the axial coordinate z in the object space ($u = 8\pi z\sin^2(a_0/2)/\lambda$), u_M is the normalized optical offset of the detector axial off-focus offset M ($u_M = 8\pi M\sin^2(a_d/2)/\lambda$), λ is the wavelength of the laser, a_0 is the semi-numerical aperture angle of the objective L_o, a_d is the semi-numerical aperture angle of the converging lenses L_1, L_2, and L_3, and v_D is the normalized radius of the pinholes radius r_D ($v_D = 2\pi r_D\sin(a_d)/\lambda$).

The intensity responses $I_A(v, u, -u_M)$, $I_B(v, u, +u_M)$, and $I_C(v, u)$ are shown in Figs. 1(e), 1(f), and 1(d), respectively. It can be seen from Fig. 1 that when the detectors D_1 and D_2 were out of the focal plane of the converging lens, the intensity responses $I_A(v, u, -u_M)$ and $I_B(v, u, +u_M)$ shifted from the intensity response $I_C(v, u)$, and the offset was determined by u_M. The peak intensities of the axial off-focus intensity responses $I_A(v, u, -u_M)$ and $I_B(v, u, +u_M)$ are weaker than that of the on-focus intensity response $I_C(v, u)$, but their shapes are consistent.

To improve CM's spatial resolution and axial focusing accuracy, we processed intensity responses $I_A(v, u, -u_M)$ and $I_B(v, u, +u_M)$ by a correlation product and differential subtraction. Here, correlation is defined as the intensity product of two signals with equal reverse offsets. The intensity responses $I_R(v, u, u_M)$ and $I_D(v, u, u_M)$ can be expressed as Eqs. (7)-(8).

$$I_R(v,u,u_M)=I_A(v,u,-u_M)\times I_B(v,u,+u_M) \tag{7}$$

$$I_D(v,u,u_M)=I_A(v,u,-u_M)-I_B(v,u,+u_M) \tag{8}$$

Figure 2(a) shows intensity response $I_D(v, u, u_M)$ obtained using the differential subtraction of intensity responses $I_A(v, u, -u_M)$ and $I_B(v, u, +u_M)$. It can be seen from Fig. 2(a) that $I_D(v, u, u_M)$ has a positive and negative bipolar responses and has a large slope at the zero-crossing point precisely corresponding to the focal plane of the objective, it means that CDCM has a better axial focusing accuracy than CM. Figure 2(b) shows intensity responses $I_A(v, u, -u_M)$ and $I_B(v, u, +u_M)$. Figure 2(c) shows intensity response $I_R(v, u, u_M)$ obtained by a correlation product processing of intensity responses $I_A(v, u, -u_M)$ and $I_B(v, u, +u_M)$. It can be seen from Fig. 2(c) that the width of the main lobe of the CDCM intensity response $I_R(v, u, u_M)$ decreased both in u-axial and v-lateral direction owing to the product, it means that CDCM has a higher spatial resolution than CM.

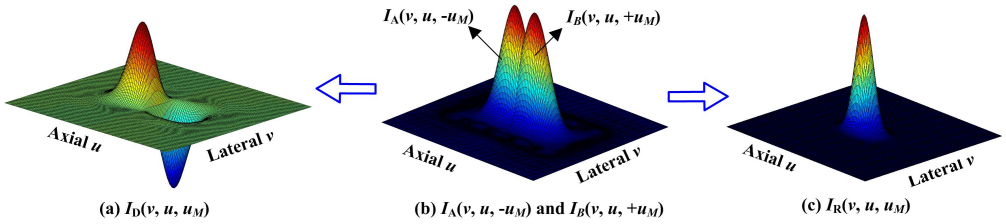

Fig. 2. Intensity responses. (a) Intensity response $I_D(v, u, u_M)$ obtained using the differential subtraction of intensity responses $I_A(v, u, -u_M)$ and $I_B(v, u, +u_M)$ (b) Intensity responses $I_A(v, u, -u_M)$ and $I_B(v, u, +u_M)$ (c) Intensity response $I_R(v, u, u_M)$ obtained by a correlation product processing of intensity responses $I_A(v, u, -u_M)$ and $I_B(v, u, +u_M)$.

In the imaging process of CDCM, two imaging mode of CDCM-correlation mode and CDCM-differential mode can be selected. The CDCM-correlation mode measures the sample by a point-by-point and layer-by-layer scan with the extreme point of the CDCM intensity response $I_R(v, u, u_M)$. The CDCM-differential mode measures the sample by a single layer scan with the linear segment of the CDCM intensity response $I_D(v, u, u_M)$. The CDCM-correlation mode can improve the CM's axial and lateral resolutions and the CDCM-

Optics EXPRESS

differential mode can improve the CM's axial focusing resolution. These two modes can be combined to improve the spatial resolution of CM.

3. Simulation analysis

To evaluate the CDCM's property, the improvements of the lateral resolution, axial resolution and axial focusing accuracy are simulated, where the axial measuring accuracy is defined as the sample axial position measuring accuracy of an optical system Assuming that the excitation wavelength λ = 405 nm, the numerical aperture of the objective Lo is NA = 0.95, v_D = 3, and u_M = 5.21 for Eqs. (1)-(6), and the system signal to noise ratio (SNR) is 200:1, the simulations are shown in Figs. 3-5.

To evaluate the CDCM's improvement of lateral resolution, we simulate the lateral edge intensity response of a height-step. The height of the step is

$$h(r)=\begin{cases}8, r>0\\ 0, r<0\end{cases} \tag{9}$$

where r is the lateral position of the step. The objective is focused at h = 8, and the intensities I_A, I_B, and I_C for $r\in(-0.4, 0.4)$ are shown in Fig. 3.

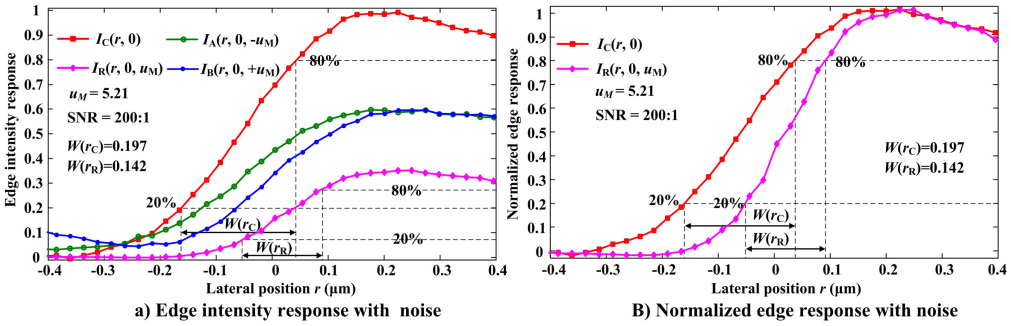

Fig. 3. Comparison of the simulated CDCM and CM lateral edge intensity responses. (a) Lateral edge intensity responses of CDCM and CM. (b) Normalized lateral edge intensity responses of CDCM and CM.

The rising edge width of the lateral edge intensity response is determined by the lateral resolution of imaging system, and the rising edge width is narrower, the lateral resolution is better. Here, we define the lateral interval corresponding to the normalized intensity from 0.2 to 0.8 as the rising edge width to evaluate the lateral resolution improvement. It can be seen from Fig. 3(a) that the rising edge widths $W(r_C)$ for CM and $W(r_R)$ for CDCM are $W(r_C)$ = 0.197 μm and $W(r_R)$ = 0.142 μm, respectively. This means that the lateral resolution of CDCM is improved by 27.9%, compared with that of CM.

To evaluate the CDCM's improvement of axial resolution, we simulate the axial intensity responses $I_A(0, z, -u_M)$, $I_B(0, z, +u_M)$, and $I_C(0, z)$, in axial direction using Eqs. (1)-(6). The simulation results are shown in Fig. 4.

Optics EXPRESS

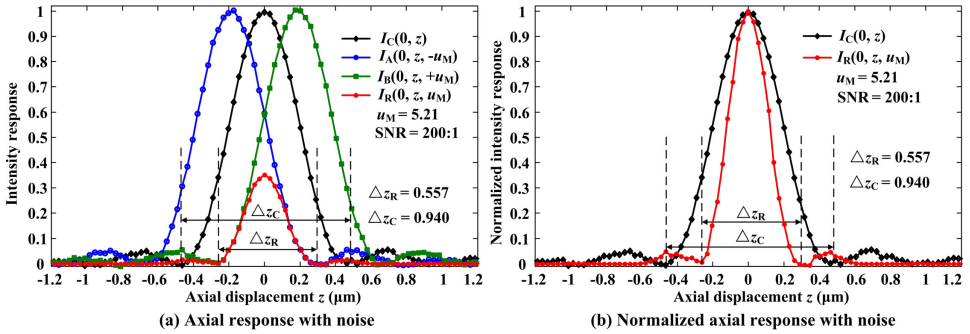

Fig. 4. Comparison of the simulated CDCM and CM axial intensity responses. (a) Axial intensity responses of CDCM and CM. (b) Normalized axial intensity responses of CDCM and CM.

The width of the axial intensity response's main lobe is determined by the axial resolution of imaging system, and the main lobe's width is narrower, the axial resolution is better. It can be seen from Fig. 4(b) that the main lobe widths of the CDCM and CM axial intensity responses are Δz_R = 0.557 μm and Δz_C = 0.940 μm, respectively. This means that the axial resolution of CDCM is improved by 40.7%, compared with that of CM.

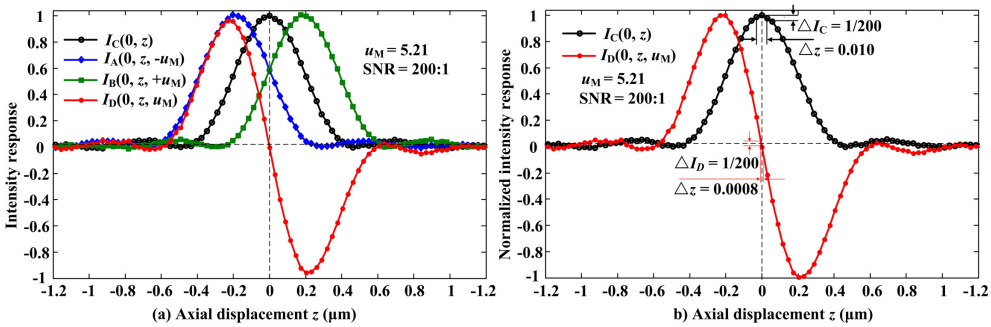

Fig. 5. Comparison of the simulated CDCM and CM axial focusing intensity responses. (a) Axial focusing intensity response of CDCM and CM. (b) Normalized axial focusing intensity response of CDCM and CM.

The simulation results of axial focusing intensity response $I_C(0, z)$ for CM and axial focusing intensity response $I_D(0, z, u_M)$ for CDCM-differential imaging mode obtained by Eqs. (1)-(6) are shown in Fig. 5. It can be seen from Fig. 5(a) that the zero-crossing point *O* exactly corresponding to the focus point of the CDCM system is in the middle of the most sensitive linear segment of $I_D(0, z, u_M)$, and the zero-crossing point *O* and its linear segment near point *O* have a large slope, which means that the intensity responses near point *O* are very sensitive to variations of the axial position and could be used for the high-precision focusing and measurements on the sample surface. The CM focusing process is conducted by the peak of the bell-shaped axial intensity response curve $I_C(0, z)$. The slope of the peak position is zero, which means that the intensity responses near the peak position are very insensitive to variations of the axial position and are not suitable for high precision focusing. As shown in Fig. 5(b), for the same intensity variations ΔI_C = 1/200 and ΔI_D = 1/200, the axial position variations of CM and CDCM are Δz = 0.8nm and Δz = 10nm, respectively. Therefore, the CDCM axial focusing and measurement capabilities are significantly improved owing to its best sensitivity and linearity near the zero-crossing point.

4. Experimental setup and analysis

The above theoretical simulations indicate that CDCM significantly improved the spatial resolution and axial focusing accuracy of CM. To further verify the CDCM effectiveness, a

Optics EXPRESS

CDCM experimental device was constructed based on the schematic shown in Fig. 1. A semiconductor laser with a wavelength of 405 nm (Thorlabs Inc. CPS405) was used as the light source, a two-dimensional piezoelectric ceramic nano-positioning system (PI Inc. P542) with a closed-loop resolution of 0.4 nm was used as the lateral sample scanning stage, a piezoelectric ceramic nano-focusing *z*-driver (PI Inc. P725) with a closed-loop resolution of 0.75 nm was used as z-axis scanning device, a 50 × flat-field apochromatic objective lens (OLYMPUS) with pupil diameter of 6.8mm and NA of 0.95 was used as the objective, and three identical doublet achromatic lenses with a focal length of 175 mm were used as the converging lenses L_1, L_2, and L_3. The diameter of pinholes P_1, P_2, and P_3 (NewPort) was 20 μm. The normalized off-focus offset u_M was 5.21, and the corresponding actual off-focus offset M was 890 μm.

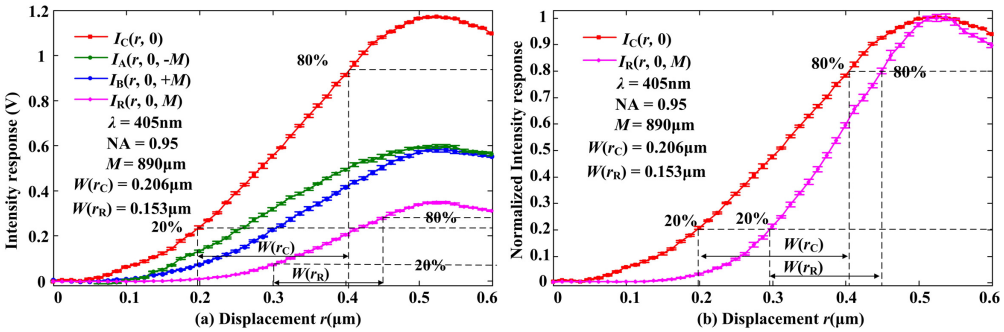

Fig. 6. (a) Measured CDCM and CM lateral edge intensity responses. (b) CDCM and CM normalized lateral edge intensity responses $I_R(r, 0, M)$ and $I_C(r, 0)$.

To evaluate CDCM's lateral resolution, we employed the CDCM and CM systems to scan the straight edge of a grid sample coated with a Co reflecting film. We measured the same position of the grid sample 10 times. The measured CDCM and CM lateral edge intensity responses $I_A(r, 0, -M)$, $I_B(r, 0, +M)$, $I_C(r, 0)$, and $I_R(r, 0, M)$ are averaged over 10 measurements and the standard deviations for this 10 measurements are given in the form of the error bar, shown in Figs. 6(a) and 6(b). The normalized lateral edge intensity responses $I_R(r, 0, M)$ and $I_C(r, 0)$ are shown in Fig. 6(b). As shown in Fig. 6(b), the average number of rising edge widths of CDCM and CM lateral edge intensity responses are $W(r_R) = 0.153$ μm and $W(r_C) = 0.206$ μm, respectively, and the lateral resolution of CDCM is improved by 25.7%, compared with that of CM, which is in good agreement with the simulation results shown in Fig. 3(b).

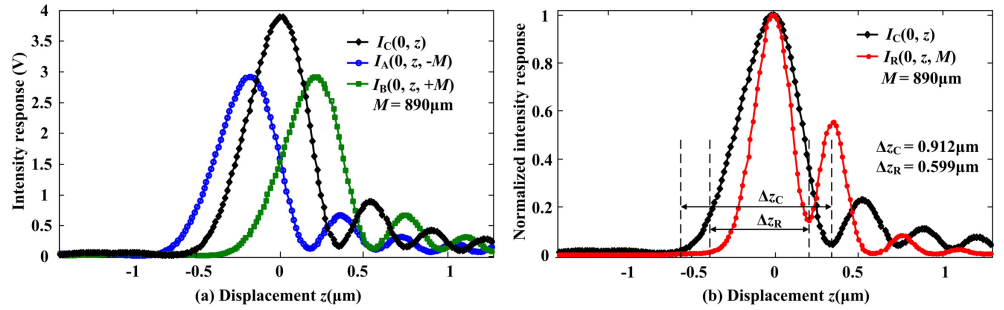

Fig. 7. (a) Measured CDCM and CM axial intensity responses. (b) CDCM and CM normalized axial intensity responses $I_R(0, z, M)$ and $I_C(0, z)$.

To evaluate CDCM's axial resolution, we employed the CDCM and CM systems to scan a mirror along the optical axis. The measured axial intensity responses $I_A(0, z, -M)$, $I_B(0, z, +M)$, and $I_C(0, z)$ are shown in Fig. 7(a). The normalized axial intensity responses $I_C(0, z)$ and $I_R(0, z, M)$ are shown in Fig. 7(b). Figure 7(b) shows that the main lobe widths of axial

Optics EXPRESS

intensity responses $I_R(0, z, M)$ and $I_C(0, z)$ are Δz_R = 0.599 μm and Δz_C = 0.912 μm, respectively, and the axial resolution of CDCM was improved by 34.3%, compared with that of the CM, which is in good agreement with the simulation results shown in Fig. 4(b).

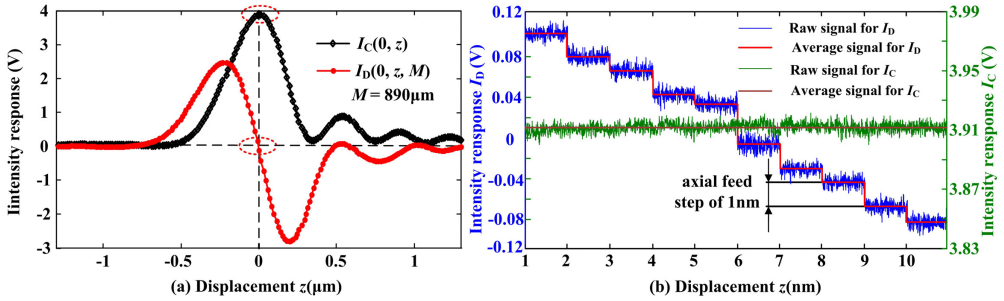

Fig. 8. (a) Measured CDCM and CM axial focusing intensity responses. (b) Intensity responses of CDCM and CM to the axial feed of 1nm.

To evaluate CDCM's axial focusing accuracy, we employed the CDCM and CM systems to scan a mirror along the optical axis. As shown in Fig. 8(a), the measured CM's axial focusing intensity response $I_C(0, z)$ and CDCM's axial focusing intensity response $I_D(0, z, M)$ are in good agreement with the simulation results shown in Fig. 5(b). And, the slope of the intensity peak position of $I_C(0, z)$ is zero, i.e., this peak position is very insensitive to variations of the axial position, the slope of the zero crossing position of $I_D(0, z, M)$ is large, i.e., this zero crossing position is very sensitive to variations of the axial position The actual intensity responses measured by $I_D(0, z, M)$ and $I_C(0, z)$ are shown in Fig. 8(b), when the nanometer-precision objective scanning system moved with an axial feed step of 1 nm. Figure 8(b) shows that CDCM could clearly discriminate the sample with an axial feed of 1 nm, while the CM can't discriminate that. Therefore, the axial focusing resolution for the CDCM-differential mode is better than 1 nm.

To verify CDCM's three-dimensional imaging capability, we employed atomic force microscope (AFM), CDCM, and CM to measure the three-dimensional profiles of standard step samples that have nominal step heights of 100 nm. As the lateral and axial resolutions of the AFM are both smaller than 1 nm, the step profile measured using an AFM can be used as a standard profile. The difference between the profiles measured by the CDCM and AFM and that measured by the CM and AFM are employed to verify the CDCM's improvements on the three-dimensional imaging capability.

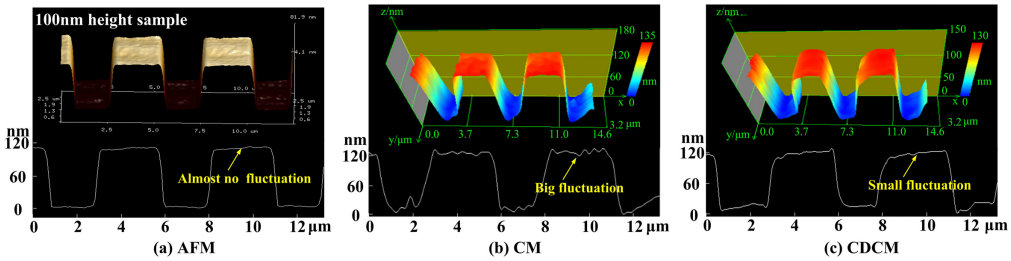

Fig. 9. Profiles of the step samples measured by AFM, CDCM, and CM. (a)Profiles of the samples that have a height step of 100 nm, measured by AFM. (b) Profiles of the samples that have a height step of 100 nm, measured by CM. (c) Profile of the sample with 100-nm height step measured by a CDCM-correlation method.

Figure 9 shows the three-dimensional profiles, two-dimensional profiles, and step heights of the standard step samples measured by AFM, CDCM, and CM. Figures 9(b) shows the profile of the step sample with nominal height step of 100 nm, that were measured by a point-by-point and layer-by layer scan with the extreme point of the CM axial focusing intensity response. Figure 9(c) shows the profiles of the step sample with nominal height

Optics EXPRESS

steps of 100 nm, measured by the CDCM-correlation mode. It can be seen from Figs. 9(a) and 9(b) that the step profile measured by CM has obvious fluctuation at the top and bottom of the height step, which is different from the profile measured by AFM. It can be seen from Figs. 9(a) and 9(c) that the fluctuation of the profile measured by CDCM at the top and bottom of the height step is very small, which is close to that measured by AFM. Therefore, CDCM provides a significantly improved axial focusing accuracy, compared with CM. In addition, the slope of the step edge measured by CM is obvious different from that by AFM, while the slope of the step edge measured by CDCM is close to that measured by AFM. Therefore, CDCM provides a significantly improved lateral resolution, compared with CM.

The lateral resolution of CDCM can improved by more than 20%, and axial resolution can improved by more than 30%, almost equivalent to pupil filtering, tight focus and super-resolution image restoration algorithm, but CDCM will not cause serious light loss as these technologies. This resolution of CDCM cannot match 4PI、divided-aperture confocal microscopy (DACM), confocal theta microscopy (CTM), dual-axis confocal microscopy (DCM), and confocal self-interference microscopy (CSIM) right now, but CDCM has a much simpler structure, and more convenient to be used, so it has a higher practical value

5. Conclusions

In conclusion, we proposed a CDCM approach that provides high spatial resolution and nano-precision axial focusing resolution with a simple structure. Theoretical analyses and experimental results show that the CDCM improved the lateral and axial resolutions of the CM by more than 20% and more than 30%, respectively, for CDCM and CM with the same parameters. The axial focusing resolution was significantly improved to 1 nm. Moreover, the CDCM differential subtraction measurement mode was used to directly perform a three-dimensional profile measurement with a nanometer precision by a single layer fast scan. Therefore, CDCM reveals a novel approach to improve the CM spatial resolution and axial focusing accuracy.

Funding

National Natural Science Foundation of China (NSFC) (61635003, 61475020,51535002) and National Key R&D Program of China (2016YFF0201005).